

Catchment precipitation processes in the San Francisco valley in southern Ecuador: combined approach using high-resolution radar images and in situ observations

Andreas Fries · Rütger Rollenbeck · Fabian Bayer ·
Victor Gonzalez · Fernando Oñate-Valivieso ·
Thorsten Peters · Jörg Bendix

Received: 22 September 2013 / Accepted: 19 May 2014 / Published online: 3 June 2014
© Springer-Verlag Wien 2014

Abstract The precise estimation of precipitation quantities in tropical mountain regions is in great demand by ecological and hydrological studies, due to the heterogeneity of the rainfall distribution and the lack of meteorological station data. This study uses radar images and ground station data to provide the required high-resolution precipitation maps. Also wind data are taken into account, due to its influence on the precipitation formation and to demonstrate the relation between synoptic wind, topography and the precipitation distribution inside small mountain valleys. The study analyses the rainfall distribution and amounts of 4 days inside the San Francisco Valley, a small catchment in the tropical Andes of southern Ecuador, representing different seasons and the typical atmospheric flows, which are correlated to the annual precipitation map. The results show that the rainfall distribution and amounts are generally defined by the wind direction and velocity, besides the topographic location in relation to the main barriers and pathways. The dominant wind direction causes

a division of the catchment in a wetter eastern and a dryer western part. Moreover, the annual seasons are reversed; the main rainy season for the eastern part occurs between June and August, while the western part reaches the precipitation maximum between January and March. This may have influence on the species composition at the different slopes and the annual hydrological cycle inside the catchment.

1 Introduction

To monitor precise precipitation intensities and quantities, radar systems have become very important, especially for flood forecast, hydrological models and ecological investigation, due to the higher spatial resolution compared with rain-gauge networks (e.g. Germann et al. 2009; Wang and Chandrasekar 2010). Mountain regions still pose difficulties for radar systems because of their limitations in this complex terrain. Besides the increasing attenuation of the radar systems with increasing range and the earth curvature, the local topography affects the precise rainfall estimation (e.g. Szturc et al. 2011). The re-evaporation of hydrometeors underneath the radar beam can hardly be detected, and each obstacle (clutter) within the radar beam produces a contamination of the signal, leaving little or no useful information in these shielded regions (e.g. Germann and Joss 2004). Furthermore, the process of rainfall formation is much more complex in mountains due to the stronger interaction between moisture transport, differential surface warming, synoptic wind field and the local mountain breeze system (Daly et al. 2007; Foresti and Pozdnoukhov 2012). The challenge to climatologists is to improve the analysis methods and to provide robust

Responsible editor: C. Simmer.

A. Fries (✉) · R. Rollenbeck · F. Bayer · V. Gonzalez ·
J. Bendix
LCRS, Department of Geography, Faculty of Geography (FOG),
University of Marburg, Deutschhausstr. 10, 35032 Marburg,
Germany
e-mail: andy_fries@gmx.de; aefries@utpl.edu.ec

A. Fries · V. Gonzalez · F. Oñate-Valivieso
Departamento de Geología y Minas e Ingeniería Civil (DGMIC),
Hidrología y Climatología Working Group, Universidad Técnica
Particular de Loja, San Cayetano Alto, Loja, Ecuador

T. Peters
Institute for Geography, University of Erlangen, Kochstr. 4/4,
91054 Erlangen, Germany

algorithms to compensate these limitations (Villarini and Krajewski 2010).

In mountain areas, the rainfall distribution and amounts vary significantly under different atmospheric flows, wherefore wind data have to be taken into account, because the local topography and the location within the valley relative to blocking barriers modify the spatial and temporal rainfall distribution (e.g. Johansson and Chen 2005). As Houze et al. (2001) described in their study, mountains modify the general baroclinic circulation, which can produce intensive rain and rapid run-off in narrow valleys. The mountain chains force the air to uplift and the water vapour condenses, producing heavy rainfall.

In mountains, the precipitation distribution is a function of the stability conditions, wind speed, perpendicularity of the flow to the terrain and the height of the mountain ridges (Foresti and Pozdnoukhov 2012). Under unstable atmospheric conditions (convective cloud formation), the distribution depends on whether the convection is thermally induced or caused by mechanical lifting over the level of free convection. During thermally induced flows, convection occurs at the mountain tops, because smaller scale mechanisms, such as the diurnal local circulation (mountain valley breeze), become important, too (Panziera and Germann 2010). If the convection is forced orographically (mechanical lifting), thunderstorms are triggered on the upwind slopes, enhancing the precipitation on this side of the mountain (Foresti and Pozdnoukhov 2012).

Under stable conditions (advective moisture transport), the spatial distribution primarily depends on whether the upstream flow is blocked or unblocked. If wind speed is high and perpendicular to the mountain chain, unblocked situations are common, which means that the air flows directly over the mountain chains. The precipitation is enhanced at the lower windward slopes and decreases towards the interior of the mountain chain. If wind speed is lower and/or not directly perpendicular to the mountain chain, blocked situations are more frequent, which means that air flows around the mountain chain, shifting the humidity further upstream. This leads to lower rainfall amounts at the windward slopes; maximum values are observed further upstream of the mountain barrier (e.g. Houze et al. 2001).

Rainfall intensities are higher when wind direction is perpendicular to the mountain barrier, due to the direct orographic lifting, leading to a faster production of hydrometeors. Normally, air saturation and the formation of raindrops have a spatial and temporal delay. However, during orographic precipitation events, the fast production of hydrometeors results from “riming” or “coalescence”. “Riming” is a microphysical process, where supercooled cloud water, “formed by the upwind motion over the windward slope, could attach themselves to precipitation

particles” (Rotunno and Houze 2007), making the particles heavier and shorten the time of raindrop generation. “Coalescence” is the warm cloud equivalent of the riming mechanism below the 0 °C level, where cloud water is collected by the existing raindrops (e.g. White et al. 2003). The raindrops fall out before they are advected over the mountain chain (barrier), which leads to the typical rainfall distribution under unblocked conditions, with highest rainfall amounts at the lower windward slope and decreasing to the interior of the mountain chain (e.g. Houze et al. 2001).

The precipitation amounts depend on the wind velocity and the water vapour content inside the air. For the same atmospheric water content, stronger winds cause higher precipitation amounts, because humidity transport towards the mountain ridge is more effective and also the vertical velocity of the air, forced by the mountain chain, is higher (Panziera and Germann 2010).

Little is known hitherto in tropical high mountains regarding rainfall distribution and amounts because meteorological station data are scarce and mostly limited to valleys (Barry 2008). Furthermore, radar systems are generally too expensive for developing countries. To overcome these limitations and to approximate the real precipitation amounts at surface, many studies try to interpolate the scarce point observations as a function of altitude (e.g. Hutchinson 1998a, b; Daly et al. 2007). However, precipitation–elevation relationships vary not only between region and aspect, but also between precipitation events. Hence, time scales have to be determined using specific gradients for each region, slope and exposure (e.g. Smith 2003). Even this improved approach is still sensitive to the heterogeneity of the station network and therefore has a limited general applicability (Rollenbeck and Bendix 2011).

In tropical high mountains, especially rainfall distribution at the micro-scale is required, as for example in small mountain valleys, to manage the water supply for the local population, for flood forecast as well as for agricultural and sustainable land-use questions (e.g. Delrieu et al. 2009). Since a few years, cost-effective X-Band radars are available as an alternative for developing countries (e.g. Local Area Weather Radar, LAWR; Jensen 2002), which also mitigate the resolution constrictions of other radar systems due to its shorter wavelength (Wang and Chandrasekar 2010). Using these instruments, rainfall in small mountain catchments can be detected adequately if sufficient ground measurements are available to calibrate the images (e.g. Germann et al. 2006; Delrieu et al. 2009).

In 2002, a X-Band LAWR radar from DHI (Dansk Hydrologisk Institut) was installed at the Cerro del Consuelo in South Ecuador (Rollenbeck and Bendix 2006, 2011) and in 2005, the hard- and software of the LAWR instrument

upgraded to provide high-resolution images of $100\text{ m} \times 100\text{ m}$ per pixel. The DHI LAWR is a modified marine radar, which does not provide a direct calculation of rain intensity/rate (R), because its sensitivity changes significantly over time. Therefore, only digital numbers (dimensionless) are stored, which must be calibrated by means of rain-gauge measurements. To date, the high-resolution images of this radar have not been used for quantitative representation of the rainfall distribution in small mountain valleys. The previous investigations focused on regional rainfall distribution and amounts to determine the annual seasons and large-scale rainfall formation processes by generating monthly and annual maps of the wider surroundings.

Other studies deal with radar rainfall measurements in steep mountain valleys (e.g. Germann et al. 2009; Gabella et al. 2012), but these investigations use expensive Doppler-Radars, which also measure the radial wind velocity and R can be calculated directly based on stable Z - R relations. However, these investigations were executed in the European Alps, and the spatial resolution is lower ($1\text{ km} \times 1\text{ km}$). Their results cannot be transferred to the precipitation distribution and amounts at the individual slopes in small narrow tropical mountain valleys.

Hence, the aim of the current study was to provide high-resolution ($100\text{ m} \times 100\text{ m}$) daily rainfall maps under different wind conditions for hydrological and ecological applications, and at the same time to understand typical weather situations and conditions of rainfall in the San Francisco valley, a small catchment at the eastern escarpment of the Andes in southern Ecuador. Also, interpolated synoptic wind maps are generated, using meteorological station data at the mountain ridges, to demonstrate the modifications of the general synoptic wind flow caused by the topography and to understand the resulting small-scale process dynamics. The investigation focuses on precipitation distribution and amounts by analysing 4 days with typical atmospheric flows during the annual seasons, which are finally compared with a yearly precipitation map. Thus, precipitation distribution on the individual slopes under different atmospheric flows can be explained, which have wide influence on the seasonal run-off regime. The precipitation maps should be the basis for hydrological models as well as for ecological applications at the individual slopes.

The paper is structured as follows: In Sect. 2, a general overview of the study area is given and the climatic conditions are explained. Also the data sets used are presented. Section 3 explains the necessary methodological improvements for the $100\text{ m} \times 100\text{ m}$ high-resolution LAWR images and the methods to derive the ancillary wind fields. In Sect. 4, examples are shown for the spatial rainfall distribution and variations at each slope by means

of four typical daily weather situations during the different seasons, which are related to the annual precipitation map. Also the results are discussed and validated. Finally, conclusions are drawn, and an outlook is given, where we try to identify general factors and processes responsible for the spatial rainfall distribution in time and space.

2 Study area and data

The Rio San Francisco watershed is located between the province capitals Loja (Province Loja) and Zamora (Province Zamora-Chinchipec), deeply incised in the eastern escarpment of the Andes in southern Ecuador and occupies an area of approximately 85 km^2 (Fig. 1). The altitude of the catchment ranges from $1,600\text{ m asl}$ at the outlet to $3,200\text{ m asl}$ at the highest mountain tops of the southern ridge. Centre of the investigation is the research station Estación Científica San Francisco (ECSF, $3^{\circ}58'S/79^{\circ}04'W$).

The natural vegetation in the study catchment is an evergreen tropical mountain forest covering the slopes from the valley bottom-up to the tree line ($\sim 2,700\text{ m asl}$). Above $\sim 2,700\text{ m}$, a shrub-dominated sub-páramo prevails. However, the lower parts of the north-eastern slopes are widely cleared by slash and burn activities to generate pasture land. The reader may refer to Bendix and Beck (2009) for more detailed information of the study area.

The climate is per humid with a marked altitudinal gradient in air temperature, air humidity (Fries et al. 2009, 2012), cloudiness and rainfall (e.g. Bendix et al. 2008a, b, c, 2009). The seasonal rainfall distribution at the eastern escarpment of southern Ecuador over $1,000\text{ m asl}$ shows a clear annual cycle with the main rain season from May to September and a relative dry season between November and February. However, the annual course changes on a short horizontal distance: In the intra-Andean basins, such as the basins of the city of Loja and Catamayo (Fig. 1), the rain season occurs between December and April, whereas August and September are the driest month (Rollenbeck and Bendix 2011; INAMHI 2000–2009). The city of Zamora (Fig. 1), located at the transitions zone between the eastern escarpment of the Andes and the Amazon Basin, shows the typical tropical cycle with abundant rainfall throughout the year and two maxima in April and October, associated with the movement of the intertropical convergence zone (Richter 2003).

The prevailing wind direction is from the east, due to the tropical easterlies (Emck 2007). Between January and April north-easterly winds dominate, between April and October south-easterly winds prevail. From June to September, wind direction hardly changes and highest wind speeds are observed (monthly average 5 – 15 m/s ;

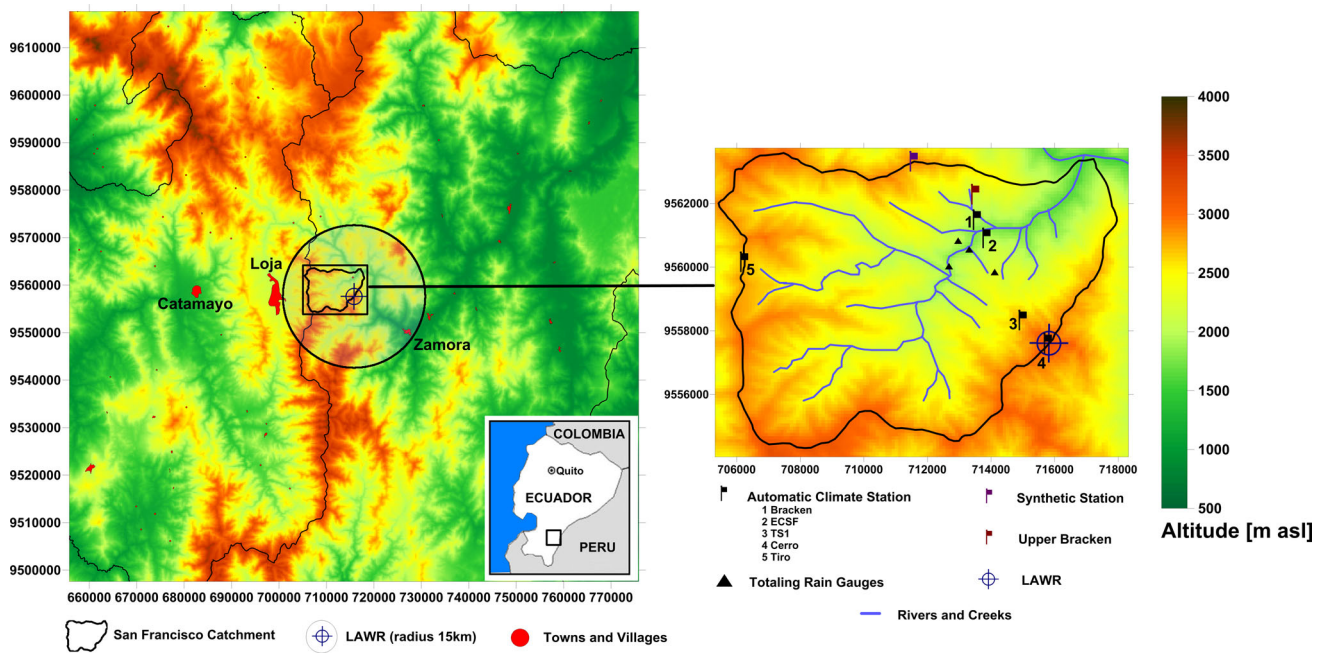


Fig. 1 DEM and study catchment with meteorological observation sites

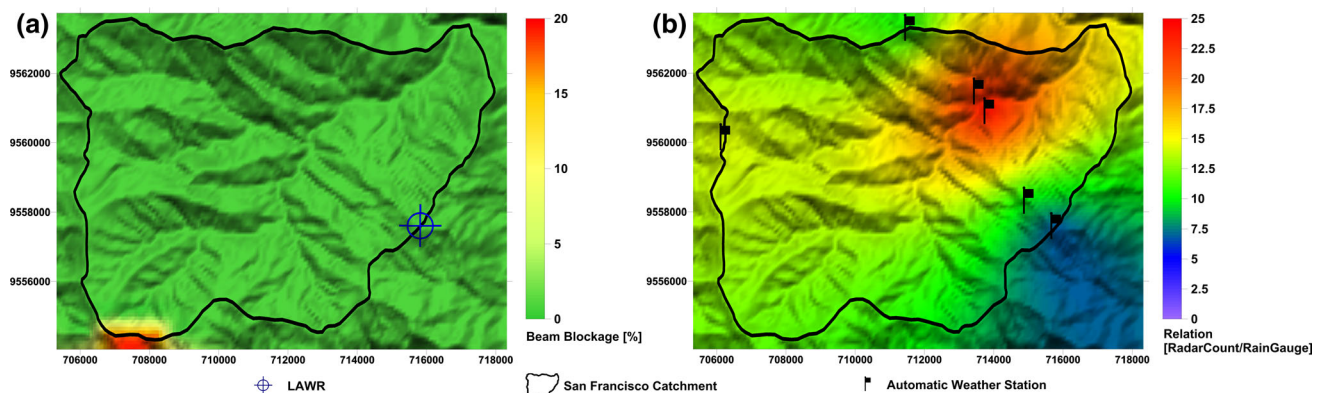


Fig. 2 **a** Beam blockage of the LAWR in the San Francisco catchment; **b** yearly relation between radar reflectivity (Z) and station data for the study period

Windhorst et al. 2013). With beginning of November, the tropical easterlies weaken and wind direction is more variable, but the proportion of the easterlies is still over 50 % during this period, displaced by short periods of westerly winds from the Pacific. Westerly flows generally bring dry and sunny weather to the study catchment (Rollenbeck and Bendix 2011), because the air masses lose their humidity at the western slopes of the Andes. Nevertheless, the formation of convective clouds and thunderstorms over the intra-Andean basins, such as the neighbouring basins of Loja and Catamayo to the west (Fig. 1), are common during these months (Vuille et al. 2000; own observations).

The radar data of the current study are obtained from a DHI LAWR (X-Band, 9.4 Ghz; Jensen 2002). It was

installed in March 2002 on the highest accessible mountain peak, the Cerro de Consuelo (3,180 m asl) in the Reserva Biológica San Francisco, only accessible by a small footpath. This location provides a very good view over the San Francisco catchment; merely a small sector in the extreme south-west is partly blocked by higher mountain tops (Fig. 2a). The LAWR is a modified marine radar, which registers the radar reflectivity (Z) in images with dimensionless counts from 0 (no reflectivity) to 254 (highest reflectivity). The antenna type is a “Fan-Beam-Antenna” (slotted wave guide) with a horizontal beam wide of 0.92° and a vertical beam wide of 10° (up and down). The rotation speed of the antenna is ~ 24 rpm (LAWR Documentation, Jensen 2004).

The LAWR automatically creates three images every five minutes, composed of ~ 125 scans. The raw analogue transmission signal is re-sampled to produce different spatial resolution ($500\text{ m} \times 500\text{ m}$; $250\text{ m} \times 250\text{ m}$; $100\text{ m} \times 100\text{ m}$) and radar ranges (60 km; 30 km; 15 km). For hydrological and ecological approaches, always the highest spatial resolution is desired. Therefore, the current study is based on the $100\text{ m} \times 100\text{ m}$ high-resolution imagery (see Fig. 1).

Due to the new hard- and software implemented by the end of 2005, an extended phase of adjustments and fixes, regarding the developed calibration and retrieval software, was required. With reference to the high-resolution data set used, the paper relies on time series for the period between September 2006 and August 2007, when the LAWR was operated with highest spatial resolution and was hardly interrupted.

To calculate the precipitation quantities from the LAWR images at surface, data from weather stations and rain gauges are needed. In the San Francisco Valley, an operational network of five automatic weather stations and four totalling rain gauges at surface level is installed (Fig. 1), which means an average distance between the stations of ~ 10 km. However, station density is higher near the valley bottom, due to the difficulties in accessibility towards higher elevation. Nevertheless, at or rather near each mountain ridge, at least one weather station is installed.

The automatic stations supply hourly data for rainfall and average hourly wind speed and direction, measured at an altitude of 2.5 m above ground (Richter 2003). Three automatic stations (ECSF: 1,957 m asl; TS1: 2,669 m asl; Cerro: 2,933 m asl) are operated since 1998 along an altitudinal gradient at the south-eastern slope (north-facing) of the San Francisco Valley. One automatic station is located on the western ridge, operating since 1999 (Tiro: 2,825 m asl). At the northern slopes, two automatic stations are installed, the Bracken station is operating since 2005 (Bracken: 1,950 m asl) and the Upper-Bracken station since 2007 (Upper-Bracken: 2,113 m asl). Using a 5-year data set (2007–2012) from the two stations at the northern ridge, a virtual data point (synthetic station) at the top of the northern ridge (Cerro-Norte: 2,880 m asl, Fig. 1) was derived.

The precipitation data of the individual automatic stations were quality checked by means of measurements from independent totalling rain gauges next to each automatic station. Furthermore, the data quality was assessed in a comparison study of all devices used in the catchment (automatic stations and rain gauges). The results show that all devices had similar precision within an error $<10\%$ (Rollenbeck et al. 2007).

To calculate the daily wind speeds and directions maps for the precipitation analyses, the wind data from the

stations on the mountain ridges are used (Cerro and Tiro) as well as the calculated synthetic values from the Cerro-Norte Station, derived from stations mentioned before. The justification for the calculation of the synthetic values at the northern ridge is given in Sect. 3.

The derivation of the rainfall distribution is based on a Digital Elevation Model (DEM) with a resolution of $50\text{ m} \times 50\text{ m}$, generated from ASTER satellite images. The single steps of the DEM creation are described in Oñate-Valdivieso and Bosque Sendra (2007). The DEM was re-sampled to $100\text{ m} \times 100\text{ m}$ to obtain the same resolution as the radar images (Fig. 1).

3 Methods

3.1 Precipitation

The LAWR radar has some operational and technical limitations, which require heavy geometrical corrections of the raw images (Jensen 2002). Also it shows strong variations in sensitivity and a continuous wear-out of the emitting device (magnetron). Correction procedures to all these problems are described in Rollenbeck and Bendix (2006, 2011); hence, only a brief description of the necessary modifications for the high-resolution images is given here:

The raw images are corrected for the decaying sensitivity with distance from centre, by applying an empirical exponential function, based on ancillary data from satellite cloud analysis (Bendix et al. 2004). The exponential function is modified according to the wear-out of the magnetron by changing the parameters of the function with time. Beam shadowing and blockage are modelled on basis of the DEM (Fig. 1), and a spatial correction map is derived, amplifying image sections in relation to the remaining beam volume (Fig. 2a). Then, a mask file is derived from the raw radar images to determine all clutter fields. The method for the clutter detection for the high-resolution images had to be improved by adjusting the thresholds for the affected grid cells, because the $100\text{ m} \times 100\text{ m}$ images show highly variable clutter fields. The different clutter patterns are caused by varying surface reflectivity during and after rainfall events, when ground wetness is changing, and by a slight instability of the antenna tower (movements caused by the wind). The detected clutter fields are subtracted from the radar image, and all affected grid cells are set to zero. The resulting blank areas are interpolated with cubic splines (e.g. Hijmans et al. 2005) to fill those areas with values estimated from the margins of the clutter fields. The more sophisticated scheme of cubic splines, compared with the original bilinear interpolation method, shows fewer artefacts,

Table 1 Relation between radar reflectivity and measured station values for the selected days and for the whole study period

Station	UTMX	UTMY	Altitude	25.09.2006	24.11.2006	08.02.2007	24.05.2007	Year
Cerro-Norte	711560	9563330	2,880	12.0	35.0	64.2	7.9	10.3
Bracken	713545	9561490	1,950	20.4	78.4	76.6	10.1	22.3
ECSF	713850	9560920	1,950					24.2
TS1	714990	9558340	2,669					9.7
Cerro	715780	9557610	3,180	2.1	30.8	90.9	19.1	6.8
Tiro	706230	9560170	2,825	29.1	27.8	16.5	12.6	14.3

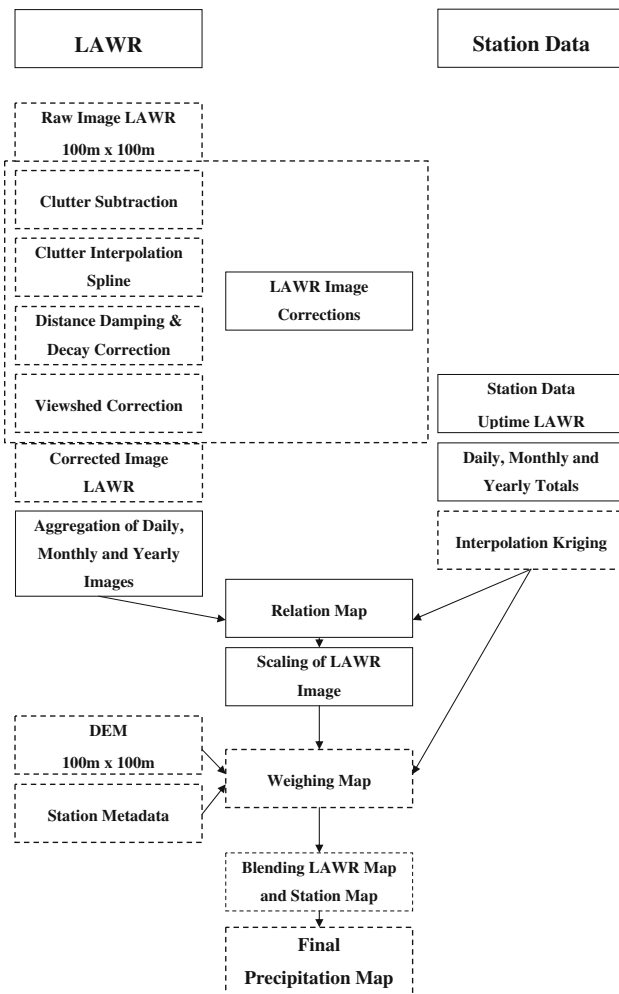


Fig. 3 Processing chain of the generation of the final precipitation maps (dotted boxes improved and changed steps; black boxes adopted steps)

especially for isolated rain storm cells, and minimises false estimates within the clutter fields (Tait et al. 2006).

After this, the 5-min real-time images are integrated into daily, monthly and annual images, which are calibrated by means of the rain-gauge measurements, using adapted relation maps. To obtain the relation maps, the measured station data at their specific location are related to the corresponding radar image grid value, and then, the

obtained relation values are interpolated to produce a relation “surface” for the whole study area. In contrast to the original scheme, which uses kriging with detrended raw data (Rollenbeck and Bendix 2011), ordinary kriging was applied, because in the smaller domain of the San Francisco watershed, the station distribution reflects the topography very well (Fig. 1). Finally, the resulting relation maps are used to calibrate the dimensionless radar images at every grid cell for the required time period (day, month and year; Fig. 2b). For each time period, a specific relation map is generated, because the relation between radar reflectivity (Z) and station values varies significantly on different time scales (see Table 1).

To make optimal use of the inherent data quality, a weighing map is derived from the spatial and altitudinal distribution of the climatic stations metadata. Thereby, the area of influence of the stations is determined by means of its horizontal and vertical location in the catchment. On basis of this weighing surface, radar data and station data are merged, giving the station data a weight of one at their precise location, and then smoothly changing over to the calibrated radar value (blending) with increasing distance from the station.

The complete processing chain for radar image calibration and the generation of the final precipitation maps is shown in Fig. 3.

3.2 Synoptic wind

Smith (2003) as well as Johansson and Chen (2005) assumed in their studies that wind speed and direction are the most important factors interpreting rainfall distribution inside mountain valleys. At the scale considered here, modelled wind fields are not reliable for the study area. Hence, the synoptic wind patterns are derived from the stations situated on the mountain ridges (Cerro: 3,180 m asl; Tiro: 2,825 m asl; Cerro-Norte: 2,880 m asl). To improve the data quality, months with more than 8 days of missing data are not considered. The daily and yearly synoptic wind directions were calculated by building vectorial averages of the hourly data; wind speed measurements are averaged.

Table 2 Average monthly and annual wind speed (ms^{-1}) and direction ($^{\circ}$) of all automatic stations inside the San Francisco Valley

Months	Cerro (3,180 m)		Tiro (2,825 m)		TS1 (2,669 m)		ECSF (1,950 m)		Bracken (1,950 m)	
	Dir	Speed	Dir	Speed	Dir	Speed	Dir	Speed	Dir	Speed
Sep-06	100	6.9	112	9.3	102	1.2	157	1.1	55	2.6
Oct-06	108	5.1	111	6.5	119	1.0	199	1.2	85	2.3
Nov-06	125	4.3	112	4.7	115	0.8	185	1.1	100	1.7
Dec-06	123	4.1	110	5.1	108	0.7	177	1.2	121	1.5
Jan-07	102	5.9	105	7.8	101	1.2	154	1.4	72	2.2
Feb-07	116	4.0	118	5.7	110	0.9	187	0.9	90	1.4
Mar-07	108	4.5	111	6.8	107	0.9	167	0.9	75	1.6
Apr-07	103	4.5	110	6.0	107	0.7	166	1.1	57	1.6
May-07	101	5.9	110	7.6	100	0.9	156	1.0	41	1.9
Jun-07	101	7.1	111	10.0	104	1.2	132	1.3	41	3.8
Jul-07	103	7.8	113	10.3	110	0.8	164	1.1	49	2.3
Aug-07	103	7.5	114	10.1	99	1.2	136	1.4	40	2.9
Year	106	5.6	111	7.5	102	1.0	164	1.1	63	2.2

Then, Kriging was applied to interpolate the station wind data as Luo et al. (2008) recommended, because this technique shows the lowest RMSE (root-mean-square error) compared with other interpolation methods. Luo et al. (2008) conclude that co-kriging is the best method, using the elevation as a co-variable, due to the dependency of wind speed on elevation. However, McVicar et al. (2010) found in their study that wind speed decreases faster at higher than at lower elevations. This is also true for the study area where no direct relationship between wind speed and elevation is observed. Other factors such as the location in relation to the barrier ridge, convergence and divergence of air inside the mountain valley are more important. By comparing average monthly wind speeds and directions of the automatic stations, the relation of the topography and the wind field becomes evident. This is shown in Table 2, where highest mean monthly wind speeds are always measured at the Tiro Station (2,825 m asl), which is not the highest station in the study area but strongly affected by Venturi-effects, causing the channeling of the air through the small side valleys up to the western mountain pass. Furthermore, lowest wind speeds are not observed near the valley bottom but at the TS1 station, which is located at 2,669 m asl on the south-eastern slope. Therefore, ordinary kriging was applied, due to the small RMSE differences compared with the co-kriging technique (Luo et al. 2008).

3.3 Synthetic station values (Cerro-Norte)

For the northern ridge, no precipitation and wind data are available; hence, synthetic values are calculated. The calculation of synthetic values is in accordance with the work

of New et al. (2000), where synthetic station values had to be calculated, because the spatial interpolation of the required variable was not feasible using only the existing station data. Furthermore, an extension of the temporal coverage for some stations was needed to integrate them into the analysis. New et al. (2000) developed an empirical relationship to calculate the variable for the required point, obtaining a higher spatial resolution, longer temporal coverage and higher fidelity of the resulting maps. A similar method was also used in previous studies calculating air temperature and air humidity in the study catchment (Fries et al. 2009, 2012). Withal altitudinal gradients were derived from measured station data to extend the existing time series and obtain higher spatial resolution of the resulting maps. The procedure assumes that the relation between the stations is stable over time.

The calculation of synthetic precipitation amounts at the Cerro-Norte station (2,880 m asl) was necessary, because the mountain ridges around the catchment produce clutter in the raw radar images, and no direct rainfall estimate is available for these parts. This leads to over-oscillations of the interpolation algorithm, when constructing the relation maps.

The precipitation amount at the Cerro-Norte station was estimated using a 5-year data set from the stations Bracken and Upper-Bracken (2,113 m asl), both installed at the northern ridge but at different elevations (see Fig. 1). From the measured rainfall data, altitudinal gradients are derived and averaged for specific wind conditions during each month and for the whole study period. Finally, the specific gradients are applied to calculate the synthetic precipitation amounts on the northern mountain ridge for the selected days and the year.

Using altitudinal gradients for precipitation estimation is only valid if the stations are located at the same slope and have the same exposure, due to the influence of the wind. Provided that these requirements are conform to the considered point, applying the gradients offers a very good approximation to the real rainfall amounts (Ochoa et al. 2013).

To derive synthetic wind data at the Cerro-Norte station, the values from the Cerro station are taken. The Cerro station is topographically undisturbed and little affected by mountain valley wind systems, due to the exposed locations on the south-eastern ridge (e.g. Ludwig et al. 2004; Jiménez et al. 2008). Although the barrier effect of mountain ridges causes wind speed to be more variable over shorter distances, both locations are situated at nearly unobstructed ridges. According to Palomino and Martín (1995), it is feasible to assign wind data to neighbouring sites if there are only small differences in elevation and if the distance between them is small (here, approximately 5 km). By validating the wind data at the Cerro station against rain cluster movements in the radar images for the considered days, it could be proved that the general atmospheric flow is nearly analogue to the measured station data (data not shown).

3.4 Validation

To estimate the accuracy of the method, a cross-validation was applied (e.g. Davis 1987; Tomczak 1998; German et al. 2009). Three automatic stations (Cerro, Bracken and Tiro) together with the synthetic values of the Cerro-Norte station are used to calibrate the daily precipitation images of the LAWR; the data from ECSF station (reference station) and TS1 station are used to demonstrate the fidelity of the results. For the annual map, all automatic station data are included for the image calibration and the results validated by means of the totalling rain gauges (Fig. 1). Also monthly precipitation maps from the LAWR images are generated and validated in the same manner as the annual map to show the overall accuracy of the calibration method.

4 Results and discussion

4.1 Wind conditions

The daily wind conditions during the study period (September 2006 to August 2007) are analysed at the Cerro station, because of its exposed position on the south-eastern mountain ridge. The undisturbed location represents the wind conditions in the lower and mid-atmosphere very well, and a Venturi-effect is negligible at this site.

As shown in Table 3, the dominant wind direction was from the east (over 70 %), mostly turned into a more east-south-easterly (ESE) direction (100°–110°, see Table 2). This weather situation was nearly unchanged in September 2006 as well as from June 2007 to August 2007, when concurrently highest wind speeds were measured (see Table 2). The austral winter (June–September) is the main rainy season inside the study catchment, and the humidity transport from the Amazon Basin is most effective, due to the high wind speeds during these months (Trachte et al. 2010).

North-easterly (NE) winds were frequent, too (over 12 %), observed mostly between November 2006 and May 2007 (Table 3). This is caused by the displacement of the intertropical convergence zone (ITCZ) to the southern hemisphere and the formation of a stationary low-pressure system over the South American subcontinent during austral summer (November to February; e.g. Richter and Moreira-Muñoz 2005). The NE winds showed dominant wind directions between 30° and 45°, but wind speeds are generally lower compared with ESE winds during austral winter (see Table 2).

The austral summer also is the relative dry season in the study catchment, when the easterly winds are periodically interrupted by slow westerly winds, bringing dry and sunny weather to the study catchment. Westerly winds occurred between November 2006 and March 2007, more frequently from the south-west (SW, over 8 %; Table 3) than from the north-west (NW, over 4 %; Table 3). These weather situations facilitate the formation of thunderstorms over the intra-Andine valleys (e.g. Vuille et al. 2000), but the slow winds sometimes carry small amounts of moisture to the study catchment.

Wind directions directly from the north (N), south (S) and west (W) were rarely observed during the study period (Table 3), probably because the mountain chains upwind of the study catchment obviate these wind directions.

4.2 Daily precipitation maps

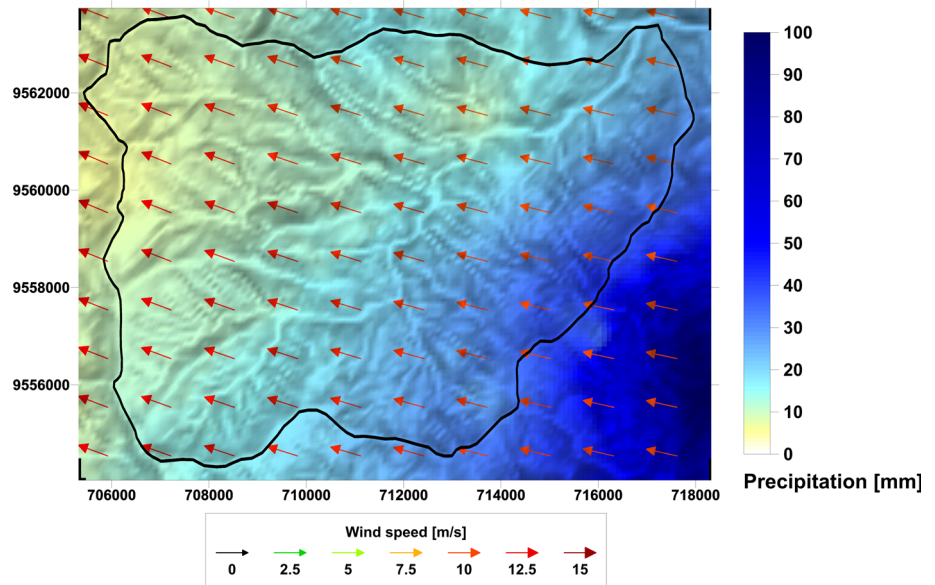
To analyse the controlling factors of the rainfall distribution and the underlying processes of rainfall formation, 4 days were selected, representing different seasons and the typical atmospheric flows. An important selection criterion was the observation of rainfall at all stations to derive the precipitation distribution. Also, the selected days had to be typical with respect to the seasonal wind conditions.

The 25 September 2006 shows the distribution during the predominant ESE flows in austral winter (Fig. 4), when the tropical easterlies are strongest and rainfall amounts highest. During this day at the Cerro station, an average

Table 3 Percentage of daily wind directions and velocity (station: Cerro; upper part); percentage of yearly precipitation accumulation between September 2006 and August 2007 (stations: Cerro and Tiro, lower part)

Sep 2006–Aug 2007	Dir	N	NE	E	SE	S	SW	W	NW	Total
Days	(#)	0	45	260	10	2	30	2	16	365
Percent	(%)	0.0	12.3	71.2	2.7	0.5	8.2	0.5	4.4	100
Dominant period		Nov–May		All the year		Nov–Mar				
Average wind speed	(m/s)	6.6		7.8		3.3				
Percent of yearly rainfall at Cerro	(%)	27.6		59.6		12.8				
Percent of yearly rainfall at Tiro	(%)	21.7		45.4		32.9				

Fig. 4 Precipitation and general wind vectors at 25 September 2006



daily wind speed of 9.7 ms^{-1} was measured, at the Tiro station 12.5 ms^{-1} , due to the Venturi-effect. However, wind speeds can reach even higher values as displayed during this specific day in austral winter (average daily wind speed during ESE winds in austral winter at Cerro: 9.7 ms^{-1} ; maximum: 16.7 ms^{-1}).

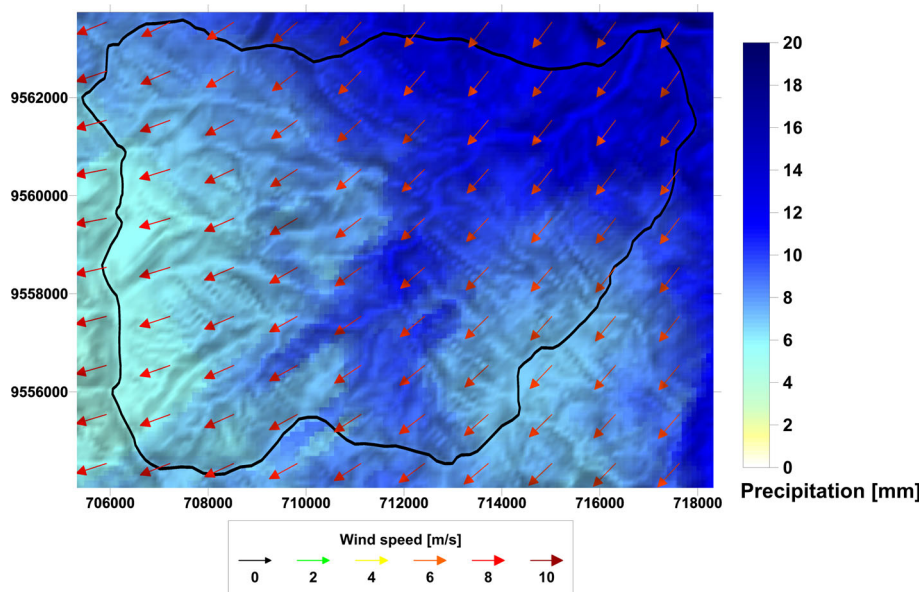
The strong ESE winds carry the moisture from the Amazon Basin up to the eastern escarpment of the Andes, intensifying condensation by orographic uplifting (e.g. Poveda et al. 2005). Generally, the moisture precipitate on the eastern mountain ridges of the Andes but where broader valleys exists, the air is conducted further up the eastern escarpment (Trachte et al. 2010). In this case, the advective moisture flow is perpendicular to the south-eastern mountain chain (Cerro station), because there are no higher mountain chains further upwind (see Fig. 1) and the south-east orientation of the main valley (Zamora River, Fig. 1), heading to the Amazon foreland, permits a flow directly to the south-eastern ridge.

A characteristic orographic rainfall distribution under unblocked conditions is visible in Fig. 4. The humid air

from the Amazon Basin is forced to ascent at the south-eastern ridge, and precipitation is enhanced on the lower windward slope, reaching highest values above 90 mm. The fast raindrop generation and fallout on the foot zone probably is not caused by the riming mechanism, because $0 \text{ }^\circ\text{C}$ level is above 4,500 m asl in the tropical Andes of Ecuador and cloud bands at the eastern Andean slopes occur between 1,000 m asl and 3,500 m asl during austral winter (Bendix et al. 2006). Therefore, coalescence in warm clouds should be the primarily mechanism on the south-eastern mountain ridge. The air, coming from the Amazon Basin, is generally near saturation and cloud formation is very common even at lower altitudes (own observations).

Up to the mountain peak of the south-eastern ridge (station: Cerro), rainfall amount decreases (39.5 mm), indicating effective rainout of the clouds at lower altitudes on the upwind slope, caused by the orographic uplifting of the humid air. Further to the northwest, terrain altitude and precipitation sharply drop to values of about 10.0 mm (stations: Bracken) as a consequence of the small-scale lee-

Fig. 5 Precipitation and general wind vectors at 24 May 2007



effect after the south-eastern ridge, where air descends and rainfall decreases. The south-eastern ridge forms the main barrier during ESE flows.

The upper eastern part of the northern ridge (south-facing) as well as the north-eastern part of the catchment shows slightly higher rainfall amounts (Cerro-Norte: 16.1 mm). They are caused by the topography of the Cerro de Consuelo mountain ridge. The barrier is lower at its eastern parts, and a higher amount of humidity can pass, leading to slightly higher rainfall amounts for this area.

At the western parts of the northern ridge as well as up the western ridge, precipitation remains below 10 mm and decreases with altitude (Tiro: 6.1 mm), because the strong barrier effect of the south-eastern ridge hinders the intrusion of moisture-laden air too far into the valley. The main part of the moisture is precipitated before and does not reach the western ridges of the Rio San Francisco watershed. Nevertheless, dense fogs are frequent at the upper western mountain ridge, because the air flowing down the leeward slope of the barrier to the valley bottom and further to the west is forced to ascend again and new clouds are formed; but now, humidity content in the air is too low for raindrop formation. By the way, fog precipitation (cloud stripping) remains undetected by radars as well as by conventional rain gauges. An estimation of the contribution of this precipitation type in the study catchment is given in Rollenbeck et al. (2011).

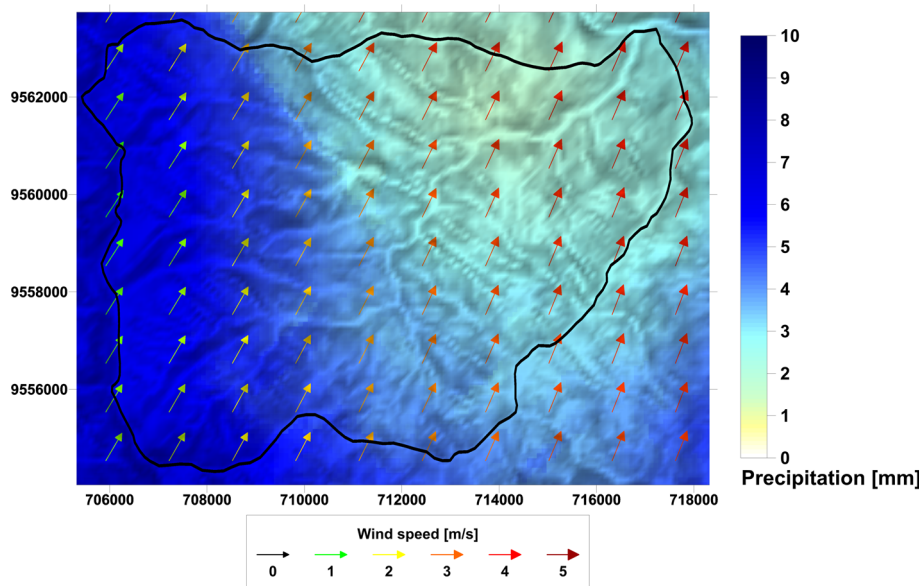
Characteristic for ESE flows is long-lasting, and sometimes intensive, drizzle for the whole study catchment.

NE flows were present at 24 May 2007 (Fig. 5). These wind conditions are frequent during the relative dry season in austral summer and at the beginning of the rainy season.

Average wind speeds are notably lower compared with the ESE winds, reaching 6.6 ms^{-1} at the Cerro station and 8.1 ms^{-1} at the Tiro station (average daily wind speed during NE winds in austral summer at Cerro: 6.6 ms^{-1} ; maximum: 11.3 ms^{-1}). Due to the lower wind speeds, the advective humidity transport from the Amazon Basin is less effective and the mountain chain located further to the north-east, upwind of the study catchment, may partially redirect the atmospheric flow to the south (possible blocked situation; e.g. Rotunno and Houze 2007; see Fig. 1). Even if wind speed is stronger and an unblocked situation occurs, the main barrier to the north-east reduces the humidity inside the air, due to the earlier rainout at the lower windward slopes. Therefore, precipitation amounts are notably lower during NE winds compared with ESE flows.

The precipitation peak is observed at the upwind slope of the north-eastern mountain ridge (Cerro-Norte) and at the north-eastern limits of the south-eastern ridge, because of the short distance to the main barrier. Nevertheless, the north-eastern ridges form a secondary barrier during this weather situation. It seems that the secondary barrier also slightly redirects the air further to the north-west and south, following the main valley of the Zamora River, because precipitation amounts are higher there. However, due to the orientation of the outlet of the San Francisco Valley to the NE, the humid air, which passed the north-eastern main barrier, can invade the catchment and the moisture is guided along the valley axes further to the south-west. Therefore, higher rainfall amounts are seen along the valley bottom-up to the southern mountain ridge. The mountain peak of the Cerro de Consuelo as well as the higher eastern parts of the south-eastern ridge does not receive the

Fig. 6 Precipitation and general wind vectors at 24 November 2006



same precipitation amounts, probably caused by the redirection of the air. Furthermore, the southern parts of the north-eastern main barrier are highest, which also effectively shield the moisture transport to the upper south-eastern ridge. The moisture flow at the main barrier is mainly guided through the centre, where peak altitudes are lower (see Fig. 1). Therefore, a higher amount of moisture is guided directly to the north-eastern mountain ridge and to the outlet of the San Francisco Valley.

The maximum precipitation value is 12.6 mm for the whole day, observed at the foot zone of the north-eastern mountain ridge. Up to the northern mountain peak, rainfall only slightly decreases (Cerro-Norte: 11.4 mm), because higher amounts of humidity still remain in the air and air ascends. Going further to the south, down to the valley bottom, rainfall amounts remain stable (Bracken: 11.4 mm) and no lee-effect is visible, because the humidity can enter the catchment, through the north-east orientated outlet and is guided along the San Francisco River. Further up to the south-eastern mountain peak, rainfall decreases (Cerro: 7 mm), caused by the two barriers lying further upwind. The western mountain ridge shows even lower rainfalls amounts (Tiro: 5.4 mm), due to the bigger distance to the barriers. The humidity is reduced progressively with increasing distance, and inside the valley, the wind guides the humidity further to the south-west.

Characteristic for this weather situation is long-lasting, but less intensive, drizzle for the whole study area.

The 24 November 2006 shows a characteristic weather situation with SW winds during the relative dry season (Veranillo del Niño, as termed by the locals; Fig. 6). The SW winds lead to a reversed distribution, associated with a convective event on the western flank of the main Andes

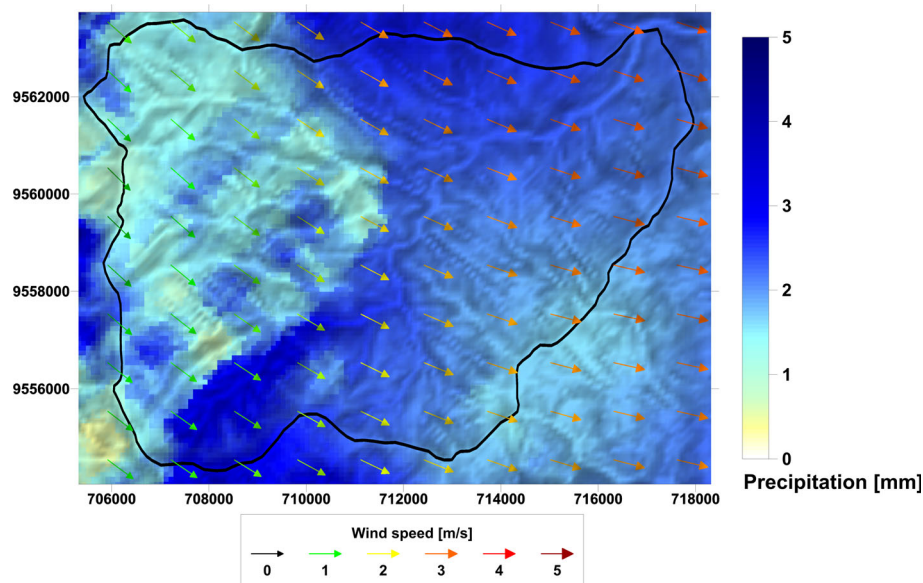
ridge, which is advected further to the east at higher elevations. The formation of convective clouds and thunderstorms over the intra-Andean basins, such as the neighbouring basins of Loja and Catamayo to the west (Fig. 1), is commonly observed during dry phases (own observations). Most likely, due to the higher air temperatures during austral summer, because warmer air can hold higher amounts of water vapour and evaporation is highest during these months, too (Fries et al. 2012).

Wind speed is even weaker with SW winds, reaching 3.6 ms^{-1} at the Cerro station and 1.2 ms^{-1} at the Tiro station (average wind speed during SW winds in austral summer at Cerro: 3.6 ms^{-1} ; maximum: 6.5 ms^{-1}). The SW wind direction does not provoke a Venturi-effect at the Tiro station, because the wind enters the catchment from the south-west and the neighbouring valley of Loja is oriented north to south.

Precipitation peaks at the upwind slope on the south-western and western ridge, with visible maximum values of about 7 mm, and decreases slowly up to the ridge (Tiro: 6.7 mm). The distribution is typical for orographic precipitation when convective air is uplifted above the level of free convection by higher mountain chains. This leads to an enhanced convection over the windward slopes of the mountain chain, where highest rainfall amounts are observed (e.g. Foresti and Pozdnoukhov 2012). Up to the mountain ridge, precipitation amounts decrease, due to the reduction in the humidity at lower elevation. During these weather situations, the western and south-western ridge forms a barrier.

Going further to the east and north-east rainfall amounts quickly decrease, caused by the lee-effect after the western barrier with descending air. Lowest values are seen at the

Fig. 7 Precipitation and general wind vectors at 8 February 2007



north-eastern mountain ridge (Bracken: 1.7 mm), not only due to the large distance with respect to the western ridge, but also to the strong barrier effect of the highest mountains of the catchment at the south-western ridge. The north-western as well as the south-western ridge shows slightly higher values than the eastern parts (Cerro-Norte: 2.3 mm; Cerro: 3.0 mm), due to the smaller distance to the barrier and the higher elevation. The topography causes orographic uplifting and enhances cloud and rainfall formation at these ridges, too.

SW winds generally bring dry and sunny weather, but if thunderstorms are forming over the neighbouring valleys, rainfall can reach the study catchment, producing intensive convective rainfall, especially at the western mountain ridge. After the western barrier, air descends and rainfall becomes less intensive with increasing distance and finally ceases. Showers and thunderstorms almost never enter the catchment basin of the San Francisco River; they tend to follow the main ridges to the north or south (own observations).

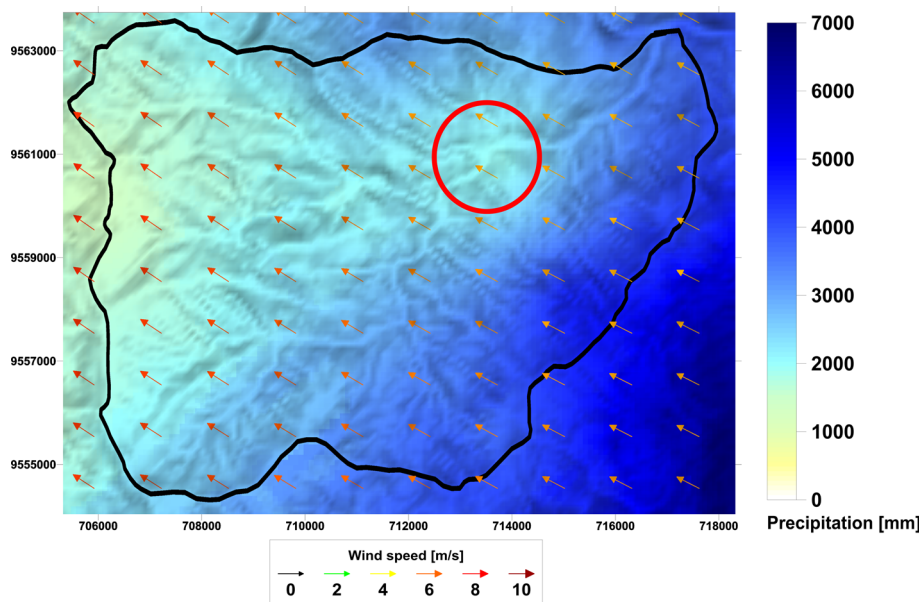
The 8 February 2007 shows a typical day with light precipitation under the influence of a NW wind during austral summer (Fig. 7). Wind speeds are generally low during NW winds, reaching 0.6 ms^{-1} at the Tiro station and 2.9 ms^{-1} at the Cerro and Cerro-Norte station during the selected day (average wind speed during SW winds in austral summer at Cerro: 3.0 ms^{-1} ; maximum: 5.1 ms^{-1}). The increasing wind speeds to the east are caused by the north-western and by the highest mountain of the south-western mountain chain, which redirect the atmospheric flow slightly to the east; but the Venturi-effect at the north-eastern and south-eastern mountain ridge is negligible (stations: Cerro-Norte and Cerro). The

Tiro station is blocked by the higher mountains further to the north, wherefore wind speeds are lower. However, air masses coming from higher and colder portions of the Andes (further to the north-east, see Fig. 1) contain less moisture, and therefore, precipitation amounts remain low.

This day is characterised by a mixture of convective and advective processes. Patches of stronger rainfall in the western and south-western part indicate showers. Highest rainfall amounts at the western part of the catchment occur near the peaks of the southern mountain ridge (3.2 mm), the most elevated part of the catchment, forming the headwaters of the San Francisco River. Here, several glacial lagoons are embedded in small basin at altitudes of 2,200–2,500 m asl to the north. Probably, this basin has accumulated warmer air due to a higher insolation and hence produces convection, which is uplifted to the mountain peaks during the daily mountain breeze.

Further to the east, convective activity seems to diminish, because the deeply incised valley does not provide sufficient warm air pools for convective cloud formation. There, advective rainfall prevails with highest amounts at the windward slope of the northern ridge (2.8 mm), forming only a subordinate barrier. Up to the north-eastern ridge and down to the valley bottom, rainfall slightly decreases (Cerro-Norte: 2.6 mm ; Bracken: 2.4 mm), because peaks altitudes are lower and the moisture in the air is not reduced severely, due to the low wind speeds. Also the local lee-effect is small. The Cerro station shows the lowest precipitation amounts (1.6 mm), because of the large distance to the northern barrier, although ridge altitudes are higher and air ascends.

Fig. 8 Annual precipitation from September 2006 to August 2007 with average annual wind speed and direction



4.3 Annual precipitation map

The annual precipitation distribution inside the study area is predominantly shaped by the influence of moisture transport from the Amazon basin (NE and ESE flows; see Table 2), carrying air and humidity up the eastern escarpment of the Andes by the tropical easterlies, intensifying condensation by orographic uplifting (e.g. Rotunno and Houze 2007). The dominant wind direction is from the ESE (Table 3), and the annual precipitation map closely resembles the distribution of the respective daily map (Fig. 8; see Fig. 4).

Rainfall totals reach 6,850 mm on the upwind slope of the south-eastern mountain ridge and 1,360 mm at the north-western limit of the watershed. The mountain peak of the Cerro de Consuelo (Cerro: 4,800 mm) shows a decrease of rainfall, indicating effective rainout of clouds at lower altitudes, probably caused by the orographic precipitation mechanism under predominant advective unblocked situations (e.g. Panziera and Germann 2010). At the leeward side of the barrier, rainfall quickly decreases and sharply drops to values of about 2,000 mm (Bracken, ECSF). The north-eastern part of the catchment as well as at the opposite slope (south-facing) at higher elevation (Cerro-Norte: 2,470 mm) shows increasing rainfall amounts, because the Cerro de Consuelo mountain chain is lower at its eastern parts. Further to the west and up the western ridge, precipitation remains below 2,000 mm per year (Tiro: 1,370 mm). The predominant wind directions from the ESE (see Table 2) cause a division of the San Francisco catchment into a wetter eastern and a drier western part.

The annual distribution is mainly governed by the prevailing advective rainfalls under the influence of the strong

easterlies. Topography, wind direction and humidity content of the air are the most important factors, influencing the rainfall distribution (e.g. Neiman et al. 2009; Foresti and Pozdnukhov 2012). At the western limit of the catchment, the topographic setting favours more convergent flows, but rainfall amounts decrease, because the air loses a lot of its precipitable water content with increasing distance to the dominant south-eastern barrier.

An interesting feature of the annual map is the relatively dry area at the eastern valley bottom, marked by a red circle in Fig. 8. The slopes to the north and south, as well as the upper valley to the west, show slightly higher precipitation amounts than inside the circle. The matter for this spatial rainfall anomaly can be explained by the topography of the south-eastern mountain chain: Where top altitudes are lower, higher amounts of moisture can pass the barrier, leading to higher precipitation on the leeward side (see Fig. 1). The neighbouring parts of the south-eastern mountain ridge do not reach the same altitude as the Cerro de Consuelo mountain peak (see Fig. 1) and a higher amount of moisture can pass the barrier. The mountain peak seems to divert moisture transport slightly to the west and north, leaving out the marked portion of the watershed. Additionally, the strong local lee-effect after Cerro de Consuelo reduces the rainfall amounts for the area located directly leeward of the mountain peak. This is confirmed by the weak wind speeds measured at the TS1 and ECSF, and the changing wind direction at lower altitudes down to the valley bottom (see Fig. 1; Table 2). Furthermore, during SW winds, this area is blocked by the highest mountains of the south-western ridge (Fig. 7) and receives lowest precipitation amounts.

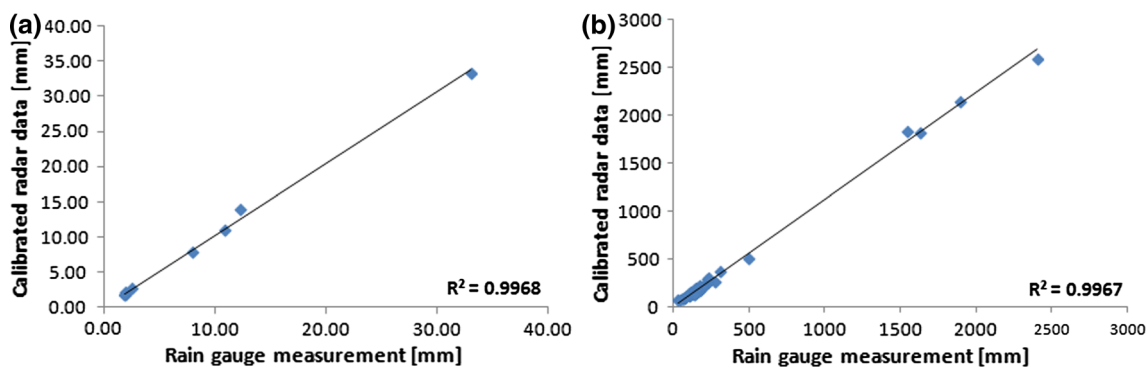


Fig. 9 Measured versus predicted precipitation values; **a** daily precipitation amounts (mm) and **b** monthly and yearly precipitation amounts (mm)

As recent field observations by the authors confirm, this area also has less water available for evapo-transpiration processes and experiences higher temperature amplitudes (Fries et al. 2009, 2012). This is also due to the conversion of the natural forest vegetation into pasture. The land cover change might have an additional impact on the hydrological cycle, the species composition and reforestation efforts at this slope.

4.4 Validation

To estimate the accuracy of the applied method, a cross-validation was employed (e.g. Germann et al. 2009). The stations for validation were selected by means of altitudinal and/or horizontal difference between the next stations integrated into the radar image calibration.

For the daily maps, the data from ECSF (reference station) and TS1 were not included in the interpolation, but used for the validation (Fig. 9a; see Fig. 1). The annual maps were validated against the totalling rain gauges, while the automatic rain gauges were used for calibration. Withal, also monthly maps were generated to show the overall accuracy of the calibration method (Fig. 9b; see Fig. 1).

This limited validation approach is viable, because the radar images are geometrically corrected by the preprocessing. This preprocessing is based on the calibration of the larger-scale images using rainfall data from the wider surroundings of the study area (Rollenbeck and Bendix 2011).

Figure 9 shows all daily (a) and monthly/yearly (b) measured precipitation data plotted against the predicted ones for the same location. The linear correlation coefficient (R^2) confirms a nearly perfect accuracy of the used method (daily: 0.997; monthly/yearly: 0.997).

5 Conclusions and outlook

The precipitation distribution in the study catchment mainly depends on the advective moisture transport from

the east, supplying the humidity for precipitation formation. Only during austral summer, the prevailing tropical easterlies are temporarily interrupted by periods of weak westerlies, bringing dry weather to the San Francisco watershed (Rollenbeck and Bendix 2011). During this period, convective clouds frequently form above the intra-Andean basins, which partially enter the study catchment from the west. Local convective cloud formation leading to rainfall in the study area was rarely observed during the study period. Probably, the mountain–valley circulation inhibits the build-up of larger pools of warm air convective cloud, and rain formation is almost completely restricted to the southern mountain ridges.

The rainfall distribution depends mainly on the wind direction and the topographic location in relation to the main barriers and pathways. Highest precipitation amounts are always shown at the lower windward slopes of the respective barrier under the different wind directions. At the leeward side of barriers, air descends, leading to partial evaporation of the clouds and a fast decrease in precipitation. The precipitation accumulation maximum is to the east as a consequence of the main barriers (south-east resp. north-east), because there, significant portions of the moisture content of the air are lost. Therefore, the catchment is divided into a wetter eastern and a drier western part.

The typical annual cycle of the study area is described in several publications (e.g. Bendix et al. 2008a). The main rainy season occurs during austral winter (May to September) with maximum values in June, but the Tiro station at the western ridge reaches its maximum in April. Lowest precipitation is observed from November to February, the relative dry season, but the Tiro station reaches its minimum in September.

The different annual precipitation cycle at the western ridge (Tiro station) can be explained now, because of its location next to the intra-Andean mountain basin of Loja (Fig. 1). The thunderstorms forming over intra-Andean

valleys have stronger influence for the western mountain ridge, so this part of the catchment receives highest rainfall amounts during the austral summer months. The difference is also shown in Table 3 by comparing the percentage of yearly rainfall accumulation of the Tiro station to the Cerro station. Nearly one-third of the annual precipitation amounts at Tiro station fall with westerly wind directions, whereas only ~13 % are calculated for the Cerro station under the same weather conditions. During austral winter, the easterly trade winds become stronger, but the main part of the humidity precipitates on the south-eastern ridges of the catchment. With increasing distance to the barrier, rainfall decreases and the western ridge receives much less precipitation than the eastern part. Therefore, concurrently minimum values are reached inside the intra-Andean basins and the western side of the San Francisco Valley (August, September), when maximum values are reached at the eastern part of the catchment.

The northern ridge also shows a division into a wetter eastern part and a drier western part. The eastern part is closer to the dominant south-eastern barrier and receives higher precipitation amounts, because the blocking effect is lower at this side (lower top altitudes); wherefore, altitudinal precipitation gradients are slightly positive. The western part receives lower rainfall totals, and gradients are negative, because most of the moisture is already depleted, when arriving there. Furthermore, during NE wind conditions, the north-eastern mountain ridge forms a secondary barrier and receives highest rainfall amounts.

With respect to the small drier spot at the lower north-eastern slopes (see red circle in Fig. 8), it can be assumed that the reduced rainfall amounts are caused by the topography of the dominant south-eastern barrier under the prevailing ESE winds. But the land cover changes from forest into pasture might have an additional impact. Inside the natural tropical mountain forest, water is hardly limited and temperatures are more uniform, but deforestation and the replacement by pastures change the natural climate conditions and additionally reduce the water availability for evapo-transpiration processes (Fries et al. 2009, 2012). This leads to a highly limited water availability for the species and also may modify the local water cycle, strongly affecting the primary production in an ecosystem, because the water cycle provides the main ecosystems services (e.g. nutrient availability; Breuer et al. 2013). The reduced water input can lead to a degradation of the ecosystem and can also complicate reforestation efforts (Günter et al. 2009).

As is well known, dense rain-gauge networks are necessary for hydrological and ecological applications in mountain areas (e.g. Germann et al. 2006), but to derive different gradient for each slope also require strategic locations to be covered. This is hardly feasible in high

tropical mountains and has led to the approach of using generalised vertical gradients to predict altitudinal distribution (e.g. Daly et al. 2007). While that approach may be valid for annual and possibly monthly maps, it is not appropriate for daily distributions. This study shows that gradients not only differ between slopes and exposure, but also within the same slope (northern ridge, south-facing), due to the variations in wind speed and direction, the topographic settings and the distance to barriers. The necessary high-resolution precipitation maps for ecological and hydrological applications can only be provided by radar images, especially in tropical mountains. Using the high-resolution images, the species composition at different slopes can be correlated to rainfall characteristics and run-off processes simulated more precisely.

Future investigations will focus on precipitation amounts at the individual slopes during specific atmospheric flows but changing wind velocities. This will support the hydrological models and will help to improve the alert systems of flood forecast for the local population.

In March 2014, two new meteorological radars will be installed in South Ecuador (RadarNet-SouthEcuador, RNSE). By combining the information, a precipitation composite allows for a more detailed insight into rainfall formation and distribution between the Pacific coast and the Amazon Basin. Therefore, the station network will be enhanced to ensure a reliable calibration and analysis of the radar images. This will help to analyse El Niño–Southern Oscillation events as well as changes in the regional and local precipitation distribution under ongoing deforestation and a future global warming.

Acknowledgments The current study was conducted within the framework of the DFG Research Group FOR 816 “Biodiversity and sustainable management of a megadiverse mountain rain forest in South Ecuador” and was generously funded by the German Research Council (DFG, BE 1780/15-2). The methodical knowledge of radar calibration is fundamental for the building of the radar network (RNSE), which is a cooperation project between DFG and the Provincial Government of Loja (GPL; BE 1780/31-1). Special thanks go to the Foundation “Naturaleza y Cultura Internacional” (NCI, Loja) for logistic support, the Universidad Técnica Particular de Loja (UTPL) for the support of the research activities, and the Ministry of the Environment of Ecuador (MAE) for the permission of the research.

References

- Barry RG (2008) Mountain weather and climate, 3rd edn. Cambridge University Press, Cambridge
- Bendix J, Beck E (2009) Spatial aspects of ecosystem research in a biodiversity hot spot of southern Ecuador—an introduction. *Erdkunde* 63(4):305–308
- Bendix J, Rollenbeck R, Palacios E (2004) Cloud classification in the tropics—a suitable tool for climate ecological studies in the high mountains of Ecuador. *Int J Remote Sens* 25(21):4521–4540

- Bendix J, Rollenbeck R, Göttlicher D, Cermak J (2006) Cloud occurrence and cloud properties in Ecuador. *Clim Res* 30:133–147
- Bendix J, Rollenbeck R, Richter M, Fabian P, Emck P (2008a) Climate. In: Beck E, Bendix J, Kottke I, Makeschin F, Mosandl R (eds) Gradients in a tropical mountain ecosystem of Ecuador, Ecological studies 198. Springer, Berlin, pp 63–73
- Bendix J, Rollenbeck R, Fabian P, Emck P, Richter M, Beck E (2008b) Climate variability. In: Beck E, Bendix J, Kottke I, Makeschin F, Mosandl R (eds) Gradients in a tropical mountain ecosystem of Ecuador, Ecological studies 198. Springer, Berlin, pp 280–291
- Bendix J, Rollenbeck R, Göttlicher D, Nauß T, Fabian P (2008c) Seasonality and diurnal pattern of very low clouds in a deeply incised valley of the eastern tropical Andes (South Ecuador) as observed by a cost effective WebCam system. *Meteorol Appl* 15:281–291
- Bendix J, Trachte K, Cermak J, Rollenbeck R, Nauß T (2009) Formation of convective clouds at the foothills of the tropical eastern Andes (South Ecuador). *J Appl Meteorol* 48:1–17
- Breuer L, Windhorst D, Fries A, Wilke W (2013) Supporting, regulation, and provisioning hydrological services. In: Bendix J, Beck E, Bräuning A, Makeschin F, Mosandl R, Scheu S, Wilke W (eds) Ecosystem services, biodiversity and environmental change in a tropical mountain ecosystem of South Ecuador. Ecological studies 221. Springer, Berlin, pp 107–116
- Daly C, Smith JW, Smith JI (2007) High-resolution spatial modelling of daily weather elements for a catchment in the Oregon Cascade Mountains, United States. *J Appl Meteorol Climatol* 46:1565–1586
- Davis BM (1987) Uses and abuses of cross-validation in geostatistics. *Math Geol* 19(3):241–248
- Delrieu G, Boudevillain B, Nicol J, Chapon B, Kirstetter PE, Andrieu H, Faure D (2009) Bollène-2002 experiment: radar quantitative precipitation estimation in the Cévennes-Vivarais region, France. *J Appl Meteorol Climatol* 48:1422–1447
- Emck P (2007) A climatology of South Ecuador. Dissertation, Friedrich-Alexander Universität Erlangen, Germany
- Foresti L, Pozdnoukhov A (2012) Exploration of Alpine orographic precipitation patterns with radar image processing and clustering techniques. *Meteorol Appl* 19:407–419
- Fries A, Rollenbeck R, Göttlicher D, Nauß T, Homeier J, Peters T, Bendix J (2009) Thermal structure of a megadiverse mountain ecosystem in southern Ecuador, and its regionalization. *Erdkunde* 63(4):321–335
- Fries A, Rollenbeck R, Nauß T, Peters T, Bendix J (2012) Near surface air humidity in a megadiverse Andean mountain ecosystem in southern Ecuador and its regionalization. *Agric For Met* 152:17–30
- Gabella M, Notarpietro R, Bertoldo S, Prato A, Lucianaz C, Rorato O, Allegretti M, Perona G (2012) A network of portable, low-cost, XBand radars, Doppler radar observations—weather radar, wind profiler, ionospheric radar, and other advanced applications. In: Bech J (ed) InTech, Croatia, pp 175–202. ISBN: 978-953-51-0496-4
- Germann U, Joss J (2004) Operational measurement of precipitation in mountainous terrain. In: Meischner P (ed) Weather radar: principles and advanced applications. Springer, Berlin, pp 52–77
- Germann U, Galli G, Boscacci M, Bolliger M (2006) Radar precipitation measurement in a mountainous area. *QJR Meteorol Soc* 132:1669–1692
- Germann U, Berenguer M, Sempere-Torres D, Zappa M (2009) REAL—ensemble radar precipitation estimation for hydrology in a mountainous region. *QJR Meteorol Soc* 135:445–456
- Günter S, Gonzalez P, Alvarez G, Aguirre N, Palomeque X, Haubrich F, Weber M (2009) Determinants for successful reforestation of abandoned pastures in the Andes: soil conditions and vegetation cover. *For Ecol Manag* 258:81–91
- Hijmans RJ, Cameron SE, Parra JL, Jones PG, Jarvis A (2005) Very high resolution interpolated climate surfaces for global land areas. *Int J Climatol* 25:1965–1978
- Houze RA Jr, James CN, Medina S (2001) Radar observations of precipitation and airflow on the Mediterranean side of the Alps: autumn 1998 and 1999. *QJR Meteorol Soc* 127:2537–2558
- Hutchinson MF (1998a) Interpolation of rainfall data with thin plate smoothing splines: I. Two dimensional smoothing of data with short range correlation. *J Geogr Inf Decis Anal* 2:139–151
- Hutchinson MF (1998b) Interpolation of rainfall data with thin plate smoothing splines: II. Analysis of topographic dependence. *J Geogr Inf Decis Anal* 2:168–185
- INAMHI (Instituto Nacional de Hidrología y Meteorología) (2000–2009) Anuarios Meteorológicos. Quito, Ecuador. <http://www.serviciometeorologico.gob.ec/biblioteca/>. Accessed 31 Jan 2014
- Jensen NE (2002) X-band local area weather radar—preliminary calibration results. *Water Sci Technol* 45:135–138
- Jensen NE (2004) Local area weather radar documentation. DHI-Institute for the water environment: DHI/LAWR/TN 2/10-2004 V 3.0
- Jiménez PA, González-Rouco JF, Montávez JP, Navarro J, García-Bustamante E, Valero F (2008) Surface wind regionalization in complex terrain. *J Appl Meteorol Climatol* 47:308–325
- Johansson B, Chen D (2005) Estimation of areal precipitation for runoff modelling using wind data: a case study in Sweden. *Clim Res* 29:53–61
- Ludwig FL, Horel J, Whiteman CD (2004) Using EOF analysis to identify important wind pattern in mountain valley. *J Appl Meteorol* 43:969–983
- Luo W, Taylor MC, Parker SR (2008) A comparison of spatial interpolation methods to estimate continuous wind speed surfaces using irregularly distributed data from England and Wales. *Int J Climatol* 28:947–959
- McVicar TR, Van Niel TG, Roderick ML, Li LT, Mo XG, Zimmermann NE, Schmatz DR (2010) Observational evidence from two mountain regions that near-surface winds speeds are declining more rapidly at higher elevation than lower elevations: 1960–2006. *Geophys Res Lett* 37. doi:10.1029/2009gl042255
- Neiman PJ, White AB, Ralph FM, Gottas DJ, Gutman SI (2009) A water vapour flux tool for precipitation forecasting. *Water Manag* 162:83–94
- New M, Hulme M, Jones P (2000) Representing twentieth-century space–time climate variability. Part II: development of 1901–96 monthly grids of terrestrial surface climate. *J Climate* 13:2217–2238
- Ochoa P, Fries A, Pilar M, Rodríguez-Díaz JA, Boll J (2013) Spatial estimation of soil erosion risk by land-cover change in the Andes of southern Ecuador. *Land Degrad Dev*. doi:10.1002/ldr.2219
- Oñate-Valdivieso F, Bosque Sendra J (2007) Extracción de modelos digitales de elevación a partir de imágenes ASTER para la determinación de características morfológicas de cuencas hidrográficas (in Spanish). In: Rivas R, Grisotto A, Sacido M (eds) Teledetección: Hacia un mejor entendimiento de la dinámica global y regional. XII Congreso de la Asociación Española de Teledetección, Mar del Plata, pp 457–464
- Palomino I, Martín F (1995) A simple method for spatial interpolation of wind in complex terrain. *J Appl Meteorol* 34:1678–1693
- Panziera L, Germann U (2010) The relation between airflow and orographic precipitation on the southern side of the Alps as revealed by weather radar. *QJR Meteorol Soc* 136:222–238
- Poveda G, Mesa OJ, Salazar LF, Arias PA, Moreno HA, Vieira SC, Agudelo PA, Toro VG, Alvarez JF (2005) The diurnal cycle of

- precipitation in the tropical Andes of Columbia. *Mon Weather Rev* 133:228–240
- Richter M (2003) Using plant functional types and soil temperatures for eco-climatic interpretation in southern Ecuador. *Erdkunde* 57:161–181
- Richter M, Moreira-Muñoz A (2005) Heterogeneidad climática y diversidad vegetacional en el sur de Ecuador: un método de fitoindicación (in Spanish). *Revista Peruana de Biología* 12:217–238
- Rollenbeck R, Bendix J (2006) Experimental calibration of a cost-effective X-band weather radar for climate ecological studies in southern Ecuador. *Atmos Res* 79:296–316
- Rollenbeck R, Bendix J (2011) Rainfall distribution in the Andes of southern Ecuador derived from blending weather radar data and meteorological field observations. *Atmos Res* 99:277–289
- Rollenbeck R, Bendix J, Fabian P, Boy J, Dalitz H, Emck P, Oesker M, Wilcke W (2007) Comparison of different techniques for the measurement of precipitation in tropical montane rain forest regions. *J Atmos Ocean Technol* 24:156–168
- Rollenbeck R, Bendix J, Fabian P (2011) Spatial and temporal dynamics of atmospheric water inputs in tropical mountain forests of South Ecuador. Special issue: hydrometeorology of tropical montane cloud forests. *Hydrol Process* 25(3):344–352
- Rotunno R, Houze RA (2007) Lessons on orographic precipitation from the Mesoscale Alpine Programme. *QJR Meteorol Soc* 133:811–830
- Smith RB (2003) A linear upslope-time-delay model for orographic precipitation. *J Hydrol* 282:2–9
- Szturc J, Katarzyna O, Jurczyk A (2011) Quality index scheme for quantitative uncertainty characterization of radar-based precipitation. *Meteorol Appl* 18:407–420
- Tait A, Henderson R, Turner R, Zheng X (2006) Thin plate smoothing spline interpolation of daily rainfall for New Zealand using a climatological rainfall surface. *Int J Climatol* 26:2097–2115
- Tomczak M (1998) Spatial interpolation and its uncertainty using automated anisotropic inverse distance weighting (IDW)—cross-validation/Jackknife approach. *J Geogr Inf Decis Anal* 2(2):18–30
- Trachte K, Nauß T, Bendix J (2010) The impact of different terrain configurations on the formation and dynamics of katabatic flows—idealized case study. *Bound-Layer Meteorol* 134(2):307–325
- Villarini G, Krajewski WF (2010) Review of the different sources of uncertainty in single polarization radar-based estimates of rainfall. *Survey Geophys* 31:107–129
- Vuille M, Raymond S, Keimig B, Keimig F (2000) Interannual climate variability in the Central Andes and its relation to tropical Pacific and Atlantic forcing. *J Geophys Res* 105:12447–12460
- Wang Y, Chandrasekar V (2010) Quantitative precipitation estimation in the CASA X-band dual polarization radar network. *J Atmos Ocean Technol* 27:1665–1676
- White AB, Neiman PJ, Ralph FM, Kingsmill DE, Persson POG (2003) Coastal orographic rainfall processes observed by radar during the California land-falling jets experiment. *J Hydrometeorol* 4:264–282
- Windhorst D, Waltz T, Timbe E, Frede HG, Breuer L (2013) Impact of elevation and weather patterns on the isotopic composition of precipitation in a tropical montane rainforest. *Hydrol Earth Syst Sci* 17:409–419